Chapter 10
Studying the Electronic Structure of Molecules with High Harmonic Spectroscopy

D.M. Villeneuve, J.B. Bertrand, P.B. Corkum, N. Dudovich, J. Itatani, J.C. Kieffer, F. Légaré, J. Levesque, Y. Mairesse, H. Niikura, B.E. Schmidt, A.D. Shiner, and H.J. Wörner

Abstract High harmonic spectroscopy is a tool to study the valence electronic structure of atoms and molecules. It uses the techniques of high harmonic generation, in which a femtosecond laser ionizes the gas sample and XUV radiation is emitted in the forward direction. The XUV intensity, phase and polarization contain information about the orbital from which an electron was removed by the laser. High harmonic spectroscopy reveals details of electron-electron interactions, motion of electronic wave packets, and can follow a chemical reaction.

D.M. Villeneuve (✉) · J.B. Bertrand · P.B. Corkum
Joint Attosecond Science Laboratory, National Research Council of Canada and University of Ottawa, 100 Sussex Drive, Ottawa, Ontario K1A 0R6, Canada
e-mail: david.villeneuve@nrc.ca

J.B. Bertrand
e-mail: Julien.Bertrand@nrc-cnrc.gc.ca

P.B. Corkum
e-mail: Paul.Corkum@nrc-cnrc.gc.ca

N. Dudovich
Department of Physics of Complex Systems, Weizmann Institute of Science, Rehovot 76100, Israel
e-mail: Nirit.Dudovitch@weizmann.ac.il

J. Itatani
Institute for Solid State Physics, The University of Tokyo, Kashiwa, Chiba 277-8581, Japan
e-mail: jitatani@issp.u-tokyo.ac.jp

J.C. Kieffer · F. Légaré · B.E. Schmidt
Institut National de la Recherche Scientifique INRS-EMT, 1650, boul. Lionel-Boulet, Varennes, Quebec J3X 1S2, Canada

J.C. Kieffer
e-mail: kieffer@emt.inrs.ca

F. Légaré
e-mail: legare@emt.inrs.ca

B.E. Schmidt
e-mail: schmidtb@emt.inrs.ca

L. Plaja et al. (eds.), *Attosecond Physics*, Springer Series in Optical Sciences 177,
DOI 10.1007/978-3-642-37623-8_10,

© Springer-Verlag Berlin Heidelberg 2013

10.1 Introduction

In recent years, high harmonic generation (HHG) has developed into the main tool of attosecond science. It has permitted the production of attosecond pulses [1], the observation of molecular dynamics [2] and the imaging of molecular orbitals with Ångström resolution [3]. HHG is most simply understood in terms of the three-step model: a molecule exposed to a strong laser field is tunnel ionized, the liberated electron is then accelerated by the field oscillations which can force it to recollide with the parent ion [4]. Recollision is the common step of most strong field processes that permit the observation of dynamical events with attosecond temporal and Ångström spatial resolution [5].

Measuring and understanding the electronic structure and correlated dynamics of matter on its natural time scale represents the main thrust of ultrafast laser science. Understanding the correlated nature of multi-electron systems indeed represents one of the major scientific challenges [6]. Electron correlations affect essential properties of complex systems ranging from configuration interactions in molecules to cooperative phenomena in solids, like superconductivity. Our knowledge of the electronic structure of matter originates from several decades of research on photoionization and photoelectron spectroscopy [7–9], mainly driven by the development of synchrotron-based sources. Recent advances in strong-field physics have opened an alternative approach to probing both the electronic structure [3, 10] and the dynamics [2, 11, 12] of molecules using table-top laser sources. These new methods rely on the recollision of an electron, removed from the molecule by a strong laser field, with its parent ion [4]. The electronic structure of the molecule is

J. Levesque
Centre for Operational Research and Analysis, Defence R & D Canada, Department of National Defence, MGen Pearkes Building 6 CBS, Ottawa K1A 0K2, Canada
e-mail: jerome.Levesque@drdc-rddc.gc.ca

Y. Mairesse
CELIA, UMR5107, Université de Bordeaux, CNRS, CEA, 33400 Talence, France
e-mail: mairesse@celia.u-bordeaux1.fr

H. Niikura
Department of Applied Physics, Waseda University, Okubo 3-4-1, Shinjyuku, Tokyo 169-8555, Japan
e-mail: niikura@waseda.jp

A.D. Shiner
Ciena Canada Ltd., 307 Legget Drive, Kanata, Ontario K2K 3C8, Canada
e-mail: andrew.shiner@gmail.com

H.J. Wörner
Laboratorium für Physikalische Chemie, Eidgenössische Technische Hochschule Zürich, Wolfgang-Pauli-Strasse 10, 8093 Zürich, Switzerland
e-mail: woerner@phys.chem.ethz.ch

encoded in the emitted high-harmonic spectrum through the amplitude and phase of the photorecombination matrix elements [11, 13–15] .

The current understanding of processes occurring in a strong laser field relies on the strong-field approximation (SFA) [16] but its shortcomings for quantitative modeling are now becoming apparent. When the electron is far away from the ion core, its motion is dominated by the laser field and therefore its wave function is well represented by plane wave functions or the time-dependent Volkov functions. The difficulty of the coupled Coulomb-Volkov problem is usually addressed by a perturbative treatment of the Coulomb field [17]. We will show that an alternative strategy, treating the ionic potential exactly and neglecting the effect of the laser field during recombination, is very accurate, at least for atoms and small molecules.

10.2 Cooper Minimum in Argon Revealed by High Harmonic Spectroscopy

The photoionization cross section of argon atoms exhibits a prominent minimum at a photon energy around 50 eV. We will show that this minimum is also apparent in the high harmonic spectrum of argon [13]. We show that the position of the minimum is not influenced by the strong laser field that is present during the recombination process. This remarkable observation implies that high harmonic experiments can directly measure the field-free electronic structure of the target atom or molecule. Experimentally, we study the argon atom as one of the most frequently used in high-harmonic and attosecond pulse generation and we show that the position of the minimum is independent of intensity and driving wavelength. Theoretically, we develop a method to calculate high-harmonic spectra from field-free continuum functions of an effective potential. The calculation of recombination cross-sections for HHG using scattering functions has been introduced in Ref. [18]. It has subsequently been used to predict harmonic spectra of the rare gas atoms [19] and H_2^+ [20]. We show that the minimum observed in HHG in argon atoms lies close to the minimum in the photoionization spectrum that is known as Cooper minimum [21]. Indeed, the last step of HHG is similar to photorecombination of an ion and an electron. We show that our method is capable of quantitatively reproducing the position of the observed minimum in contrast to other methods using plane waves or Coulomb waves.

The experimental setup consists of a chirped-pulse amplification titanium-sapphire laser system (KM Labs), a hollow-core fiber setup for pulse compression and a vacuum chamber for generation and characterization of high-harmonic radiation. The laser system provides pulses of 2 mJ energy and 35 fs duration at a repetition rate of 1 kHz. The pulses are focused into a hollow-core fiber filled with argon to achieve self-phase modulation [22] and are subsequently compressed using chirped mirrors. The typical duration of the compressed pulses was 6–8 fs. These pulses are focused $\sim$1 mm below the orifice of a pulsed nozzle generating a supersonic expansion of argon. This setup minimizes the effects of phase mismatch and reabsorption of the high-harmonic radiation and leads to the observation

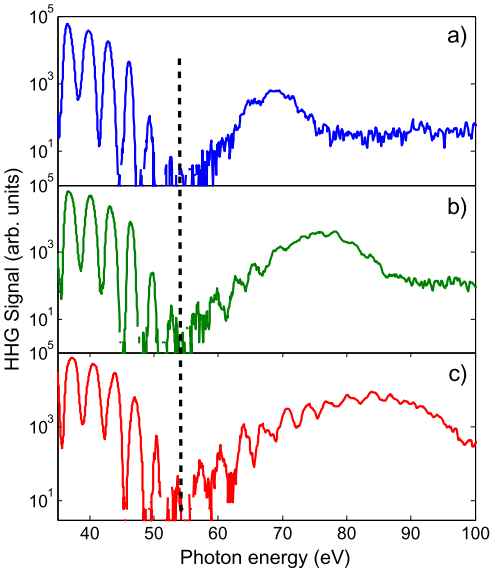

Fig. 10.1 High-harmonic spectra generated in argon using an 8 fs laser pulse centered at 780 nm. The three different panels correspond to the laser intensities 2.5×10^{14} W/cm^2 (**a**), 2.9×10^{14} W/cm^2 (**b**) and 3.5×10^{14} W/cm^2 (**c**). Adapted from [23]

of the single-atom response. The generated high-order harmonics are sent into an XUV spectrometer consisting of an aberration-corrected concave grating that spectrally disperses the harmonics and images them onto a microchannel plate detector. A CCD (charge-coupled device) camera accumulates the spectral image and transfers it to a computer. The image is integrated over the spatial dimension to provide the high harmonic spectrum.

High-harmonic spectra generated in argon using an 8 fs laser pulse centered at 780 nm at different intensities are shown in Fig. 10.1. In the region of low photon energies, the spectrum shows the usual progression of odd harmonics of the fundamental wavelength which turns into a continuum close to the cut-off. The most striking feature of the spectrum is the presence of a deep minimum around the 33rd harmonic.

Different origins are conceivable for minima in high-harmonic spectra. Minima can originate from the structure of the atom or molecule. Their position is approximately independent of the laser intensity as is the case in 2-center interference [24]. A minimum can also originate from dynamics of either the electron in the continuum or of the molecular cation following tunnel ionization and/or the action of the strong laser field. An example of continuum dynamics has been reported using a mixture of helium and neon as nonlinear medium [25]. Such minima are associated with a well defined recollision time and their location in photon energy (i.e. harmonic order) would therefore shift approximately linearly with intensity. It would also depend strongly on the wavelength of the fundamental field.

With increasing intensities the cut-off in the high-harmonic spectra shown in Fig. 10.1 extends clearly, but the position of the minimum is left unchanged. Measurements at longer wavelengths have revealed a minimum at the same photon energies as reported here [26]. This proves that the minimum observed in high-harmonic

spectra of argon is associated with the *electronic structure* of the atom rather than with its *dynamics* in the laser field and is independent of the laser source.

We find that the minimum in argon appears at 53 ± 3 eV. This is close to the observed position of the Cooper minimum in the single-photon-ionization efficiency [27]. The minimum in argon has been reported many times in the literature since the early days of HHG [28, 29]. The minimum is much deeper in our spectra because we use an ultra-short pulse that extends the cut-off and places the minimum into the plateau.

We now show that we can accurately model the recombination step in HHG using field-free one-electron procedures commonly used in photoionization spectroscopy. The potential is used to generate both the bound (ground) state and the continuum wave functions, neglecting the laser field at the moment of recombination. Without the laser field, the problem is spherically symmetric. The electronic wave function is represented as a product

$$\Psi(r,\theta,\phi) = \frac{1}{r}\phi_\ell(r)Y_\ell^m(\theta,\phi) \tag{10.1}$$

of a reduced radial wave function $\phi_\ell(r)$ and spherical harmonics. ℓ stands for the angular momentum quantum number of the electron and m its projection quantum number. An effective one-electron potential [30]

$$V_\ell(r) = \frac{\ell(\ell+1)}{2r^2} - \frac{1}{r} - \frac{Ae^{-r} + (17-A)e^{-Cr}}{r} \tag{10.2}$$

with $(A = 5.4, C = 3.682)$ is used and spin-orbit interaction is neglected. The ground state wave function (3p) is generated by diagonalizing the Hamiltonian for $\ell = 1$ on a numerical grid. The continuum functions are generated by numerically integrating the Schrödinger equation for a given (positive) kinetic energy of the electron using the Numerov algorithm [31]. The normalization is performed at asymptotically large radial coordinates including the Coulomb tail [32].

Figure 10.2 represents the bound and continuum wave functions for argon. The two-dimensional cut through the continuum wave function was obtained by summing all partial wave components from $\ell = 0$ to $\ell = 50$ that were obtained from numerical integration of the effective potential in Eq. (10.2). The continuum wave function consists of a plane wave propagating along the x axis from left to right and the superimposed scattered wave that strongly distorts the appearance of the plane wave. This highlights the problem of using plane waves to represent the continuum wave function, as we will do in future sections.

Figure 10.3 shows the log base 10 of the photoionization dipole squared as described above. The minimum at about 55 eV is evident. Also shown is the photoionization phase which is seen to have a gradual phase shift over tens of electron volts around the Cooper minimum. The gradual nature is due to the d-wave partial wave component of the transition changing sign around the minimum, but it does not have sufficient magnitude near the minimum to abruptly influence the phase.

The minimum observed in HHG occurs because the total recombination dipole goes through a minimum for a certain value of the electron's kinetic energy. This

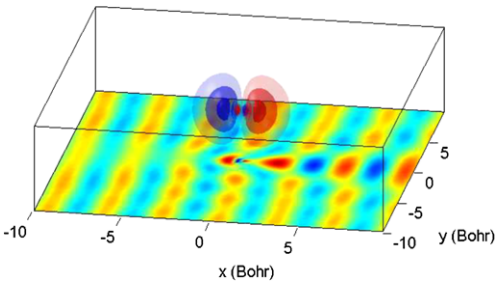

Fig. 10.2 $3p_x$ ($m_\ell = 0$) orbital wavefunction of argon and two-dimensional cut through the real part of the continuum wave function for $k = 1.8$ a.u. The atomic orbital was obtained from a quantum chemical *ab initio* calculation using the Hartree-Fock method and the cc-pVTZ basis set. *The two colors* correspond to different signs of the wave function and their intensity of color codes the amplitude. The continuum wave function was calculated from the effective potential given in the text by adding the components $\ell = 0$ to 50. *The color code*, in this later case, represents the amplitude. Adapted from [23]

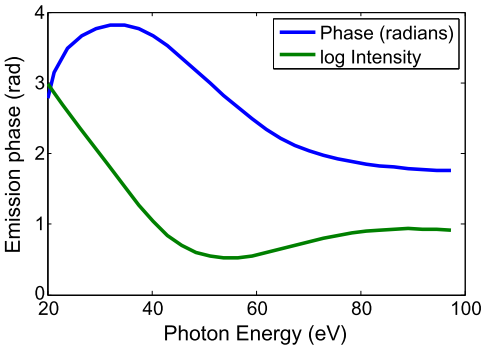

Fig. 10.3 *Green line* shows the log base 10 of the calculated photoionization cross section. The Cooper minimum near 55 eV is evident. *The blue line* shows the phase of the photoionization dipole moment. A gradual phase change of somewhat less than π occurs centered at the Cooper minimum

happens because the radial integral for the transition to d wave changes sign. Moreover, the phase of the dipole varies quickly across the minimum position. This will translate to a similar variation in the harmonic phase that should be observable in experiments using the RABBITT technique [33, 34] or mixed gases [25].

The present example enables us to directly compare the information content of a HHG spectrum with that of a photoelectron experiment. The radial integrals are identical for both cases but a photoionization cross section represents an *angle-integrated* measurement and is thus described by an *incoherent* sum over the emitted partial waves whereas HHG is an inherently *differential* technique which is expressed as a *coherent* sum over recombining partial waves. This explains why the minimum seen in HHG is much deeper than the minimum seen in photoionization.

The conversion from the electron's kinetic energy ($k^2/2$ in atomic units) to the photon energy (Ω) has been a subject of debate in recent work, some studies using $\Omega = k^2/2$, others $\Omega = k^2/2 + I_p$ [3, 35, 36]. The disagreement originates from the fact that the kinetic energy of the electron is not clearly defined at the moment of recollision because the electron is accelerated by the ionic potential. The use of

plane waves and the relation $\Omega = k^2/2 + I_p$ predicts that the minimum in argon lies around 21 eV. If the other dispersion relation is used, the minimum shifts to 5 eV, so the agreement with experiment is even worse. In the case of exact continuum functions, the dispersion relation can only be $\Omega = k^2/2 + I_p$ because the momentum k of the electron is defined at asymptotic distances from the core where the ionic potential is negligible.

The main approximations of the present method lie in neglecting the laser field which can be justified using a semi-classical argument by comparing the magnitude of the energies involved in the process. The electron corresponding to the observed minimum position has a kinetic energy of 35 eV and the ionic potential is 15.8 eV. However, the variation of the electrostatic potential of the laser field across the region where recombination takes place amounts to a few electron-Volts only. This means that the effect of the laser field on the electron at the moment of recombination is negligible and suggests that field-free continuum wave functions properly describe the region where recombination occurs.

10.3 Interchannel Coupling and the Giant Resonance in Xenon

In the previous section, we showed that a structural feature in the photoionization cross section of argon could be clearly seen in high harmonic spectra. We now extend this observation, to show that photoionization cross sections can be recorded up to 150 eV, and that the high harmonic spectrum contains features due to multi-electron processes during photorecombination, specifically interchannel couplings.

We use high harmonic spectroscopy to investigate a new class of collective electronic dynamics—induced and probed by the recombining electron. The kinetic energy of the returning electron is usually much larger than the difference between electronic energy levels of the parent ion. Consequently, inelastic scattering followed by recombination is energetically possible, as illustrated in Fig. 10.4(right). Using the xenon atom as an example, we demonstrate that such processes indeed occur and that they can locally enhance the efficiency of HHG by more than one order of magnitude. We show that such a seemingly complex pathway contributes significantly to the phase matched process. This observation uncovers a new unexpected facet of high harmonic spectroscopy—it provides access to electron correlations which are otherwise very difficult to observe. Our results suggest that electron-electron (e-e) excitations may be ubiquitous in high harmonic spectroscopy experiments. High harmonic spectroscopy gives access to multi-electron dynamics through their spectral signature, much as in photoionization studies, but it offers the additional potential of attosecond temporal resolution.

Until recently, HHG was interpreted within the single-active-electron approximation. HHG experiments in pre-formed, transition-metal plasmas by Ganeev et al. [37] observed significant enhancements of a single harmonic order. These enhancements were recently interpreted by Frolov et al. [38] to be caused by Fano autoionizing resonances and 3d-3p transitions, underlining the importance of multi-electron effects in HHG.

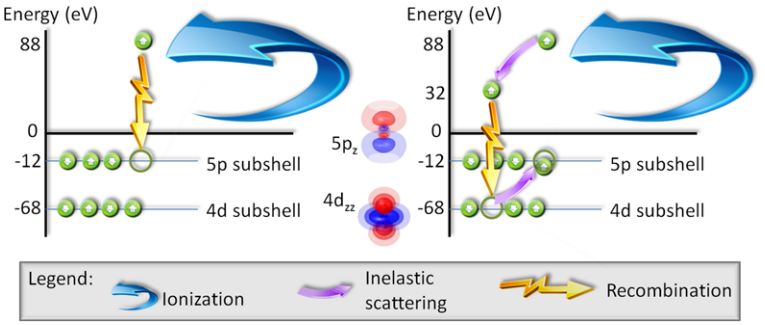

Fig. 10.4 Steps for harmonic generation. In the usual 3-step model an electron is tunnel ionized from the valance shell, accelerates in the continuum and then recombines to the state from which it came (*left*). With inelastic scattering the returning electron can promote a lower lying electron into the valance band and then recombine to the vacancy in the lower lying state (*right*). In both cases a 100 eV photon is emitted by recombination to a 5p vacancy (*left*) or a 4d vacancy (*right*). Adapted from [39]

We used a novel laser source that is almost ideal for spectroscopic studies [40–42] (see below), having a wavelength of 1.8 μm and a duration of less than 2 optical cycles. With its long wavelength, it creates a recollision electron whose energy can exceed 100 eV, even for low ionization potential systems such as small organic molecules.

HHG spectra were recorded for the noble gases, argon, krypton and xenon, using a thin phase-matched gas jet [39]. Results are shown in Fig 10.5 and demonstrate the smooth spectra that are possible with this laser source. The limit of 160 eV is imposed by the spectrometer. We now show how the photoionization cross section can be measured with these spectra. It has been shown that the three-step model for HHG [4] can be approximately factorized into three terms [3, 15, 43, 44] corresponding to ionization (I), electron propagation $W(E)$, and recombination (σ^r). Although the range of validity for this expression has not been fully explored, it is sufficiently accurate to allow us to compare the HHG spectra of Xe and Kr, both of which involve ionization from p-orbitals.

$$S(E_\Omega) = I(F,\omega)W(E)\sigma^r(E) = \mathbb{W}(E)\sigma^r(E). \tag{10.3}$$

Here $S(E_\Omega)$ is the HHG power spectrum, $E_\Omega = E + I_p$ is the emitted photon energy, E is the electron kinetic energy, ω is the laser frequency, F is the laser field, and I_p is the ionization potential. The photorecombination cross section σ^r is related to the photoionization cross section σ^i through the principle of detailed balance [43, 45]. In addition, the differential photoionization cross section in which the photoelectron is ejected parallel to the polarization vector of the electromagnetic field is the appropriate component for photorecombination. The differential cross section is determined from the anisotropy parameter β measured in the photoionization experiments, using the relation $\partial\sigma^i/\partial\Omega = \sigma^{total}(1 + \beta P_2(\cos\theta))/4\pi$ for $\theta = 0$.

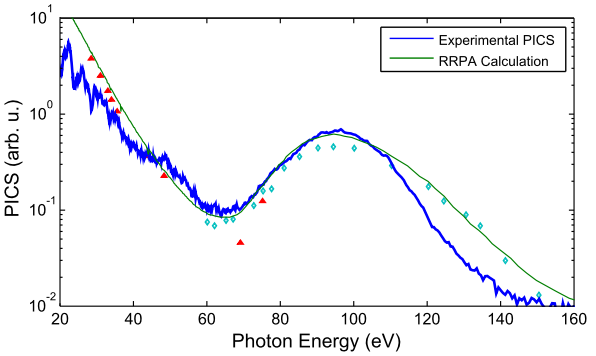

Fig. 10.5 Experimental HHG spectrum for xenon (*blue line*) obtained with a laser source with a wavelength of 1.8 μm, pulse duration of 11 fs (∼ 1.8 cycles), and intensity of 1.9×10^{14} W/cm^2. The raw xenon spectrum was divided by the spectrometer calibration. The RRPA calculation of the xenon PICS by Kutzner et al. [47] (*green line*). *The red and green symbols* are PICS measurements by Fahlmann [48] and Becker [49] respectively, each weighted using the anisotropy parameter calculated by Kutzner et al. [47]. Derived from [39]

In order to calibrate the recording system, we use the measured HHG spectrum from krypton $S_{Kr}(E_\Omega)$ and the photoionization cross section $\sigma^i_{Kr}(E_\Omega)$ from the literature [46] to accurately determine the recolliding electron wavepacket spectrum $\mathbb{W}(E)$ by setting $\mathbb{W}(E) = S_{Kr}(E_\Omega)/\sigma^i_{Kr}(E_\Omega)$, using a similar approach to that used by Itatani et al. [3]. We then divide the measured HHG spectrum for xenon with this term, to extract the photoionization cross section for xenon: $\sigma^i_{Xe} = S_{Xe}(E_\Omega)/\mathbb{W}(E)$. Because this procedure divides one spectrum by another, experimental details such as grating reflectivity and detector response cancel out. In addition, the proportionality factor [43, 45] relating σ^i and σ^r approximately cancel out when the ionization potentials are similar. The correction factor is at most a factor of 2 across the entire spectrum, telling us that the recolliding wave packet is almost flat across the spectrum. The experimentally derived σ^i_{Xe} is plotted in Fig. 10.5, together with the photoionization cross section from synchrotron experiments. The excellent agreement shows that the HHG spectrum contains detailed information about the electronic structure of atoms, imprinted through the photorecombination cross section. It is remarkable that the intense laser field can be neglected.

We now study the xenon results, shown in Fig. 10.5. The most striking feature is the pronounced peak around 100 eV. This peak is also seen in the photoionization cross section from synchrotron measurements, also shown in Fig. 10.5. This peak has been extensively studied in the context of photoionization, and led to the development of a theory that included e-e correlations during photoionization [50]. The 100 eV peak is interpreted as being due to the influence of 4d electrons, which have a large photoionization cross section in this region owing to a shape resonance. Energy-resolved measurements [49] have shown that the photoionization cross section of the 5p shell is strongly enhanced around 100 eV through e-e interactions with the 4d sub-shell.

The first step in HHG is tunnel ionization from the most weakly bound electrons, the 5p electrons in the case of xenon. The probability of tunnel ionizing a 4d electron whose binding energy is 68 eV is vanishingly small (10^{-51}). So how is it that the photorecombination process in HHG can manifest the influence of the 4d shell? Figure 10.4(right) illustrates the Coulomb interaction between the returning continuum electron and a bound 4d electron. An exchange of energy takes place, resulting in the promotion of a 4d electron to fill the 5p hole. This causes the continuum electron to lose 56 eV (the difference between binding energies of the two sub-shells), and hence to have the correct kinetic energy to experience the quasibound continuum state that enhances the 4d cross section. The decelerated electron then recombines to the 4d hole and emits a photon whose energy is the same as that of the direct channel, due to energy conservation. The smooth green curve in Fig. 10.5 is derived from a complete multi-electron calculation [47] that includes contributions from all sub-shells.

Although we have successfully predicted the observed HHG spectrum in xenon, it is not obvious that the 4d channel will be phase matched, a necessity for HHG. Does the e-e interaction cause a loss of the coherence that is necessary for HHG phase matching? A generalized HHG model [39] shows that coherence is indeed maintained. In SFA, the ion evolves with a phase given by its total energy; the continuum electron gains a phase given by the classical action. After the collisional excitation, both the ion and the continuum electron exchange energy, but the total energy remains the same, meaning that the excitation time does not affect the emission phase, and coherence is maintained.

The observation of the 100 eV peak in xenon in the HHG spectrum is striking in several ways. It reinforces the observation that the HHG spectrum is largely determined by the photoionization cross section [15, 23, 43]. In fact Frolov et al. [15] predicted that the xenon giant resonance will appear in HHG spectra. The agreement between our measured spectrum and the previously measured photoionization cross section is remarkable because it represents a clear observation of e-e correlations and excitation of the ion in HHG. Indeed, it is quite likely that collisional excitation followed by recombination to an inner shell orbital is a general phenomenon in HHG whose experimental evidence has been directly observed for the first time due to the newly developed sub-two cycle IR laser source.

10.4 High Harmonics from Aligned Molecules

It has been demonstrated in experiments with aligned molecules that the highest occupied molecular orbital (HOMO) largely determines the shape of the HHG spectrum [51]. It was shown [3] that the process of high harmonic generation could be used to form an image of a single electron orbital wave function of N_2, and that the orbitals of rare gas atoms determine the HHG spectrum [36]. These experiments are supported by calculations that show the dependence on the HOMO [52–55]. In this section, we will show that the HHG spectra from aligned N_2, O_2 and CO_2 have

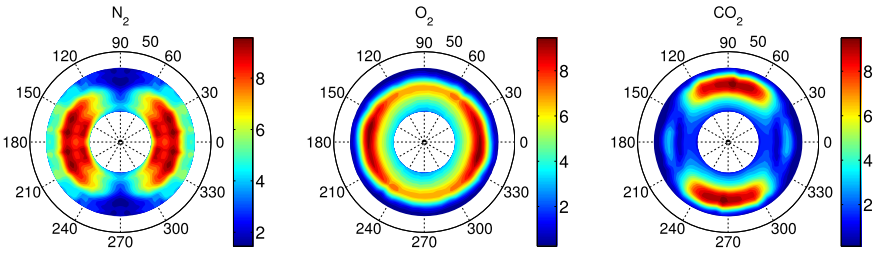

Fig. 10.6 Experimental high harmonic spectra versus angle between the molecular axis and the laser polarization, from N_2, O_2 and CO_2 molecules. *The colour scale* is the square root of the intensity of each harmonic, divided by the continuum wave function amplitude $\Omega^2 a(\Omega)$. The radius in the polar plot is the harmonic order (from 17th to 43rd), and the polar angle is the angle between the molecular axis and the laser polarization. Derived from [56]

unique features that are determined by the electronic structure of each molecule [56].

The experimental setup has been described previously [3, 57]. Briefly, N_2, O_2 or CO_2 gas was introduced into the vacuum chamber through a pulsed supersonic valve providing a gas density of about 10^{17} cm^{-3} with a rotational temperature of about 30 K. A 30 fs duration, 800 nm laser pulse with an intensity of about 5×10^{13} W/cm^2 created a superposition of rotational states, leading to periodic revivals of molecular alignment [58, 59]. The direction along which the molecular axes were aligned could be rotated by means of a half wave plate. At the peak of the rotational revival, typically 4–20 ps after the first pulse, a second, more intense, laser pulse was focused into the gas to produce high harmonics. Its intensity was approximately 1 to 2×10^{14} W/cm^2. The HHG spectra were recorded by an XUV spectrometer consisting of a variable groove spacing grating and an MCP and CCD camera.

HHG spectra were obtained for molecules aligned in 5 degree steps in the range of ± 100 degrees relative to the intense laser's polarization. The results are presented in Fig. 10.6. The value that is plotted is related to the measured intensity of each harmonic order, $S(\Omega)$, as follows.

In the three step model, the HHG response is a product of the ionization, the propagation, and the recombination. We lump together the first two steps into a term that describes the continuum wave function at the time of recombination, $a(\omega)$. The emitted signal $S(\Omega)$ is given by

$$S(\Omega) = \Omega^4 \left| a(\Omega) D(\Omega) \right|^2. \tag{10.4}$$

Here, Ω is the emitted XUV frequency, and D is the recombination dipole matrix element. The spectral amplitude of the continuum wave function $a(\Omega)$ was determined by a separate measurement of the harmonic spectrum, $S_{ref}(\Omega)$, taken from a reference atom, argon. Rather than matching the ionization potential of the molecules with individual reference atoms, we used only argon. It was shown in

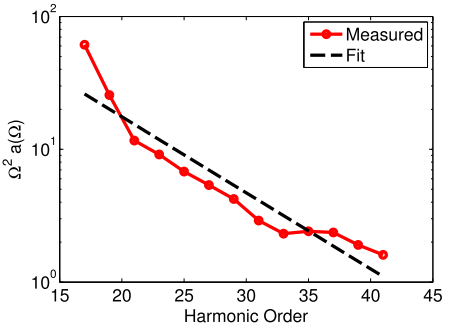

Fig. 10.7 Calibration of the continuum wave function $\Omega^2 a(\Omega)$ amplitude from the reference argon spectrum. The HHG spectrum of argon is recorded, then is divided by the calculated recombination dipole for the Ar 3p orbital. *A straight line* fit on the semilog scale is used to normalize the spectra presented in Fig. 10.6. Derived from [56]

[36] that atoms as different as He, Ne and Ar, gave essentially the same continuum wave function amplitude,

$$a(\Omega) = \frac{S_{ref}(\Omega)^{1/2}}{\Omega^2 D(\Omega)}.$$

D is evaluated using the 3p orbital of argon calculated by GAMESS [60]

The calibration $\Omega^2 a(\Omega)$ is approximately a straight line on a semilog plot [36] as shown in Fig. 10.7. We fit it to a linear function, $\Omega^2 a(\Omega) = a_1 e^{-a_2 \Omega}$, to avoid any small deviations due to structure in the argon spectrum, for example the Cooper minimum near H31 [13, 21]. Thus in Fig. 10.6 we plot $S(\Omega)^{1/2}/(\Omega^2 a(\Omega))$.

It should be noted that the alignment dependence of the ionization probability is implicitly included in these measurements. For example, we know that N_2 is more easily ionized parallel to its molecular axis, whereas CO_2 and O_2 preferentially ionize at 45° [61]. In addition, all values are integrated over the distribution of molecular angles that are present in the aligned ensemble.

Each molecule is clearly distinctive, supporting our notion that the valence electronic structure of each molecule is responsible for the HHG emission. N_2 shows strongest emission near 0°, whereas CO_2 is strongest at 90°. O_2 shows less variation with angle, but peaks broadly near 0°.

The CO_2 measurements clearly show an amplitude minimum near 0° that is conventionally attributed to two-center interference in the emission process [62–64]. The position of the minimum goes to higher order with increasing molecular angles. For the simple plane wave model, destructive interference of emission from each of the oxygen atoms occurs when $\sin(k \cdot R/2) = 0$, where $R = 2.3$ Å is the distance between the oxygen atoms, and k is the electron wavenumber (or momentum in atomic units) associated with the harmonic order. This can be written as $\cos\theta_{mol} = 2\pi/kR$. For $\theta_{mol} = 0$, the minimum should occur at H27, assuming the "dispersion relation" $\Omega = k^2/2 + I_p$. Measurements of the harmonic phase by the RABBITT technique [65] show a phase jump of about 2 radians in this region, and

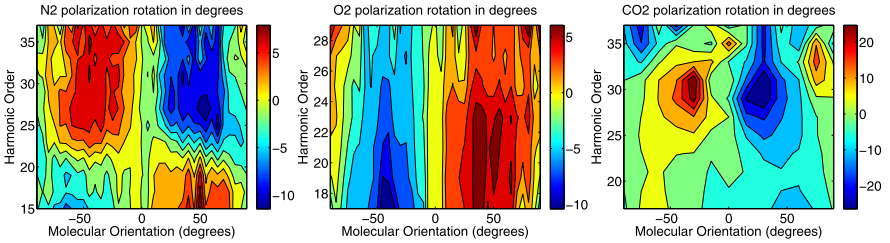

Fig. 10.8 Measurement of the polarization rotation of harmonics produced in aligned N_2, O_2 and CO_2. *The colour* represents the rotation angle from vertical in degrees. Positive values (*colour red*) mean that the emitted XUV polarization has deviated from the probe laser polarization direction, in the direction of the molecular axis. For an atom, the rotation angle will be zero. To within experimental accuracy, the emitted radiation was linearly polarized. Derived from [68]

the position of the phase jump increases with molecular angle. These observations seem consistent with a two-center interference process that depends on molecular orientation. However it should be noted that there is some disagreement in the location of the interference minimum. Kanai et al. [64] observed the minimum at H25, where Vozzi et al. [63] observed it at H33. This was attributed to an intensity dependence of the interference that is not predicted by the simple model and needs further theoretical investigation. This discrepancy has now been resolved to be due to interferences between emission from different orbitals in CO_2, notably the HOMO and HOMO-2 when the laser field is parallel to the molecular axis [11, 66].

The N_2 measurements show a minimum around H25. Interestingly, this minimum does not shift to higher orders as the molecule is rotated away from the laser polarization, and even exists in unaligned molecular samples. Measurements of the harmonic phase in randomly aligned [67] and aligned N_2 [65] show a phase jump starting at H25, also independent of angle. All these observations are in contradiction with the simple two-center interference model, which predicts a strong angular dependence of the amplitude and phase.

In order to measure the polarization state of the emitted XUV radiation, the previous setup was modified to include a pair of silver mirror at 20° and 25° angles between the grating and the MCP [68]. These mirrors acted as an XUV polarizer [69], although not with perfect extinction. As in the previous section, the direction of the molecular axis could be controlled by waveplate HWP1, and was varied in 5° steps over the range $\pm 100°$. In addition, the polarization of both pump and probe pulses was rotated by HWP2. In a typical polarimetry measurement, the analysing polarizer is rotated; in the present case we keep the analyser fixed and rotate both the molecules and the probe laser polarization. Further details of the experimental setup can be found in Ref. [68]

The results of the polarization measurement [68] for different aligned molecules are shown in Fig. 10.8. We present the polarization direction in the laboratory frame, in which the incoming laser polarization is vertical. It is also possible to present the same data in the molecular frame (not shown). As was the case for the measurement of harmonic intensity, each molecule shows a unique signature.

The polarization rotation measured in O_2, shown in Fig. 10.8(b), is rather unremarkable compared with the other molecules studied. The XUV polarization is rotated in the direction of the molecular axis, but its value is largely independent of molecular angle or harmonic order. This implies that there is no change of sign of the recombination dipole vector components.

The polarization measurements for CO_2 molecules are shown in Fig. 10.8(c). This molecule shows the greatest amount of polarization rotation of the three molecules studied. It is significant that the direction is opposite to that of O_2. The maximum rotation coincides with the harmonic order previously associated with a minimum in the harmonic spectrum in CO_2. Thus, polarimetry allows us to attribute this amplitude minimum to the component of the dipole moment that is parallel to the generating laser polarization.

The N_2 molecules in Fig. 10.8(a) show a change in behaviour between low and high harmonic orders. For the low harmonics, the polarization direction rotates in the direction of the laser polarization. The high harmonics show a rotation in the opposite direction. This remarkable feature was recently confirmed by other measurements [70]. The point at which the rotation changes sign is around H21, and this point is largely independent of angle. This almost coincides with the order at which the emission amplitude has a minimum, H25, which is also independent of angle. The minimum in amplitude indicates a minimum in the recombination dipole matrix element. The change in polarization direction indicates a sign change in the perpendicular component of the vector recombination dipole. This would seem to be contrary to the conclusion from the experimental measurements in which it seems that the perpendicular component changes sign. However the experimental results are consistent with the model interpretation where the parallel component changes sign. Since the experiment only measures the angle of the polarization modulo 2π, what seems like a rotation of say 20° could in reality be a rotation of -160°. Thus the amplitude and polarization measurements contain complementary information about the recombination dipole.

10.5 Tomographic Imaging of a Molecular Orbital

Some interpretations of quantum mechanics hold that wave functions do not exist in reality, and that only the square of the wave function has any meaning. Nevertheless scientists use the concept of wave functions to help visualize the electronic structure of atoms and molecules [71]. In particular, single-electron molecular orbital wave functions are mathematical constructs that are used to describe the multi-electron wave function of molecules. The highest lying orbitals are of particular interest since they are responsible for the chemical properties of molecules. Yet they are elusive to observe experimentally. Using the highly non-linear process of tunnel ionization in an intense, femtosecond infrared laser field, we selectively remove the highest occupied molecular orbital electron, and then recombine this electron about 2 fs later. This results in the emission of high harmonics from the molecule that contain information about the shape of the molecular orbital. By aligning the gas phase molecule

at a set of angles, the resulting HHG spectra can be tomographically inverted to yield the two-dimensional orbital wave function. The coherent interference between the free electron wave function and the molecular orbital wave function, a form of homodyne detection, enables us to see the actual wave function, not its square [3].

Only a few methods can currently "see" the highest molecular orbitals—electron momentum spectroscopy (EMS) [72] and scanning tunneling microscopy (STM) [73–75]. These experiments have provided valuable data that can be compared with various theoretical descriptions, e.g Hartree-Fock, Kohn-Sham and Dyson orbitals [76]. Other techniques such as electron scattering or x-ray diffraction measure the total electron density of the molecule, not specific orbitals. Yet it is the frontier orbitals that give the molecule its chemical properties.

HHG is usually thought of as a source of attosecond XUV photons that can be used to probe ultrafast dynamics. We will use molecular HHG not as a probe, but as a sensitive signature of the molecular orbit structure. It has been suggested that the HHG spectrum from molecules might contain information on the internuclear separation [77, 78]. We will show that, by recording a series of HHG spectra from molecules held at fixed angles, it is possible to tomographically reconstruct the shape of the highest electronic orbital, including the relative phase of the wave function.

It is possible to align gas-phase molecules in space by means of non-resonant laser fields [79]. It has been demonstrated that medium-sized molecules can be held in space in three dimensions using elliptically polarized fields [80]. Field-free alignment has been demonstrated using an adiabatic pulse that abruptly turns off [81], and by short pulses that produce rotational wavepackets that periodically rephase [82]. Furthermore, polar molecules can be oriented in a particular direction [83, 84].

A proof-of-principle experiment was performed on a simple molecule, N_2, whose highest occupied molecular orbital (HOMO) is known to be a $2p\sigma_g$ orbital. More precisely, the $2p\sigma_g$ is the Dyson orbital that is associated with ionization of N_2 to the ground state of the cation. The next highest orbitals, about 1 eV below the HOMO, are $2p\pi_u$, and so have distinctly different symmetry. Evidence for emission from lower orbitals of N_2 has been reported [85].

In the experiment [3] the output of a Ti:Sapphire laser system (10 mJ, 27 fs, 800 nm, 50 Hz) was split into two pulses with a variable delay. The first pulse served to produce a rotational wave packet in the nitrogen gas emanating from a nozzle [82]. Its intensity was low enough ($< 10^{14}$ W/cm^2) that no harmonics were generated. The second laser pulse (3×10^{14} W/cm^2) produced the HHG spectrum that was detected with an XUV spectrometer.

During the rotational revivals, there were two distinct times at which the molecules have a clear spatial orientation—parallel (4.094 ps) and perpendicular (4.415 ps) to the laser polarization [82]. We used the parallel alignment time, and rotated the molecular axis relative to the polarization of the HHG pulse using a half-wave plate. In order to remove the sensitivity of the XUV spectrometer and other systematic effects, we have normalized the N_2 spectrum to that of argon. Argon has nearly the same ionization potential as nitrogen, and so the ionization process will be very similar. The calibration used is similar to that shown in Fig. 10.7.

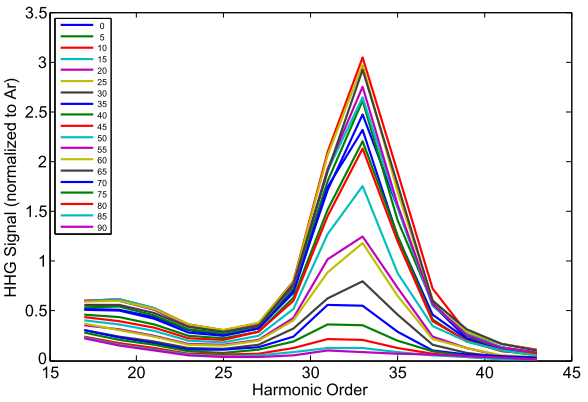

Fig. 10.9 High harmonic spectra of N_2 recorded at 5 degree increments for the angle between the molecular axis and the laser polarization direction. Each spectrum has been divided by the linearized argon reference spectrum to remove the amplitude of the recolliding wave packet. Derived from [56]

It has been shown that the three-step model for HHG [4] can be factorized into three terms [3, 15, 43, 44]. The harmonic signal will be proportional to the square of the dipole moment induced by the returning electron,

$$\mathbf{d} = \langle \psi_m(\mathbf{r}) | \mathbf{r} | \psi_e(\mathbf{r}) \rangle. \tag{10.5}$$

Here, ψ_m is the molecular orbital wave function that was ionized. The outgoing electronic wave function is a complicated Volkov wave [86], but upon return $\psi_e(\mathbf{r})$ is described by a plane wave, e^{ikx}. More recent models have described the continuum state as a field-free scattering state. For the sake of simplicity in analysis, we will use the plane wave model. For each harmonic number n, we know that the corresponding momentum k_n of the returning electron is $\hbar k_n = \sqrt{2m_e(nE_L - E_i)}$.

In Fig. 10.9 we show the high harmonic spectra recorded for aligned N_2 molecules, divided by the argon reference signal. The molecular axis has been rotated by 5 degrees between each measurement, and the fact that each spectral amplitude is different indicates the high degree of alignment achieved.

We now go on to show that the HHG signal can be tomographically inverted to yield a picture of the molecular orbital. We will assume that the laser polarization axis is in the x direction, and that the molecular axis is at an angle θ with respect to x. For a non-planar molecule, this angle can be replaced by the Euler angles that will completely describe its orientation. We then use a rotated version of the wave function to represent the rotated molecule, $\psi_m(\mathbf{r}, \theta)$.

From Eq. (10.5) the dipole magnitude for the n-th harmonic can be written as an integral,

$$\mathbf{d}_n(\theta) = \int_{-\infty}^{\infty} \int_{-\infty}^{\infty} \psi_m(\mathbf{r}, \theta) \mathbf{r} e^{ik_n x} dx dy \tag{10.6a}$$

$$= FT\left\{ \int_{-\infty}^{\infty} \psi_m(\mathbf{r}, \theta) \mathbf{r} dy \right\} \tag{10.6b}$$

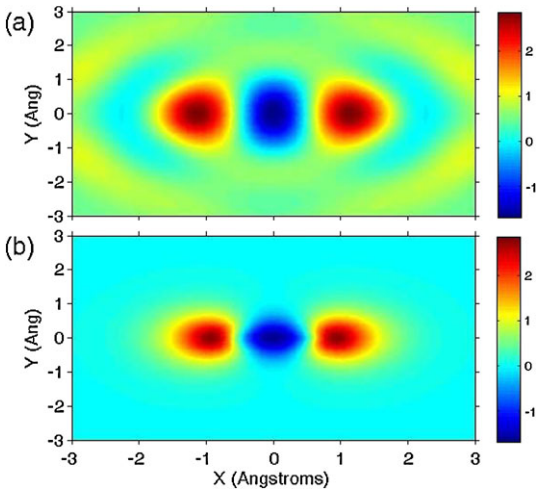

Fig. 10.10 (**a**) Highest occupied molecular orbital of N_2 as reconstructed using the high harmonic emission in Fig. 10.9. Assumptions about a phase jump near H25 and the polarization of the emission were made. (**b**) *Ab initio* calculation of the $3\sigma_g$ orbital of N_2. Derived from [3]

where we have dropped the third dimension z for clarity. Note that $\mathbf{d}$ is a complex vector. It can be seen that this is a spatial Fourier transform in direction x of an integral along y of the molecular wavefunction.

The Fourier Slice Theorem [87] shows that the Fourier transform of a projection P is equal to a cut at angle θ through the two-dimensional transform F of the object. This is the essence of computed tomography based on the inverse Radon transform. Our dipole is the Fourier transform of a projection of the wave function, and so the parallel between the HHG process and computed tomography is uncanny.

The result of the tomographic deconvolution is shown in Fig. 10.10. The upper panel shows the experimental reconstruction, while the lower panel is the calculated shape of the $3\sigma_g$ orbital of N_2. Note that the colour scale includes both positive and negative values, indicating that we are measuring a wave function as opposed to the square of the wave function. The lobes at which the wave function passes through zero are well reproduced in the reconstruction.

It may seem that quantum mechanics forbids the observation of a wave function [71]. Whereas a single quantum system cannot be observed, an ensemble of quantum systems can be measured [88]. In addition, we effectively record the dipole matrix elements of a transition between two states of the system, Eq. (10.5). Since this is an expectation value of a Hermitian operator, it is an observable in quantum mechanics. We determine the molecular orbital wave function to within an arbitrary phase, with a normalization constant and a DC term, because it is effectively a homodyne measurement; part of the bound state electron wave function is removed by the laser, and then interferes with itself when it recombines.

The spatial resolution is limited to the electron wavelength corresponding to the highest attainable harmonic order. This is determined by the ionization potential E_i and the intensity at which the molecule ionizes (not necessarily the peak laser intensity). For $I = 2 \times 10^{14}$ W/cm^2 at 800 nm wavelength, $nE_L = 38$ eV and $\lambda_e = 2$ Å. By going to longer wavelengths, such as through the use of optical parametric amplifiers, the cutoff energy is increased. For a laser wavelength of 1.8 μm, $\lambda_e = 0.9$ Å,

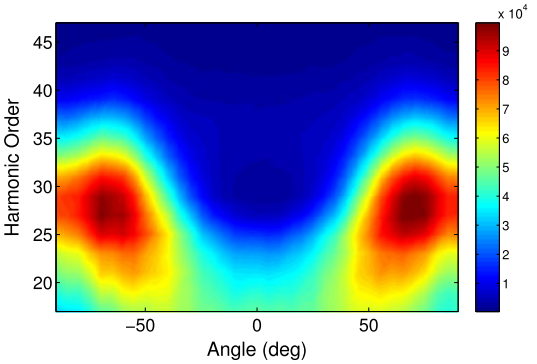

Fig. 10.11 High harmonic intensities for aligned CO_2 molecules using elliptically polarized laser radiation. The HHG signal was obtained for ellipticities for which the spectrum was reduced by 1/3, averaged for both left and right ellipticities. This removes the effect of the nodal planes, since the recolliding wave packet returns at an angle to the nodal plane

and the highest spatial frequency component is $k = 7\ \text{Å}^{-1}$. This is usually sufficient to resolve typical molecular orbitals [89].

The mathematical underpinnings of this reconstruction technique have been studied in more detail in [90, 91]. Rather than considering just a single molecular orbital, the more detailed approaches consider all electrons in the system to be indistinguishable, leading to concepts of Dyson orbitals and electron exchange upon recombination. These factors have an effect on the interpretation of the reconstruction, and lead to even better agreement between theory and experiment than shown in Fig. 10.10.

10.6 Tomographic Reconstruction of CO_2 Molecular Orbital

In the previous section we showed how one can create an image of a single molecular orbital wave function in the case of N_2 molecules. In this section we use a similar approach to a different molecule, CO_2. The shape and symmetry of the CO_2 HOMO (Π_g) is quite different from that of the N_2 molecule (Σ_g). The presence of nodal planes in Π_g symmetry makes the interpretation more difficult. In addition, for a perfectly aligned molecule at 0 degrees, the ionization along the nodal plane direction results in a node in the outgoing continuum electron wave function. Therefore the returning continuum wave function will have a nodal plane, violating the assumption of a plane wave. This violation does not occur at angles other than 0 and 90 degrees. Nevertheless, it makes the reconstruction more complicated. A reconstruction of the HOMO of CO_2 was performed by Vozzi et al. [92].

To get around this difficulty, we performed an experiment with aligned CO_2 molecules using elliptically polarized 800 nm laser radiation [93]. High harmonic spectra were recorded for each molecular alignment angle, at a range of laser ellipticities. The HHG signal was obtained for ellipticities for which the spectrum was reduced by 1/3, averaged for both left and right ellipticities. The experimental results are shown in Fig. 10.11.

As was the case for the reconstruction of the N_2 wave function, the HHG spectrum from CO_2 was divided by the HHG spectrum from reference argon atoms.

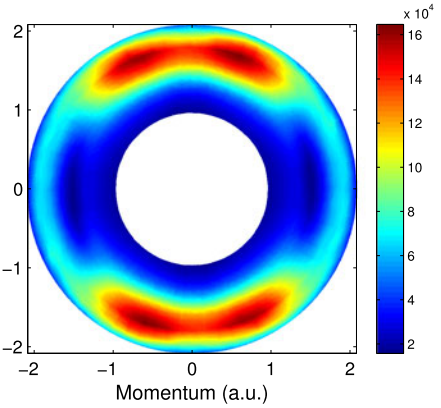

Fig. 10.12 Polar plot of the square root of the CO_2 signal from Fig. 10.11, normalized by the HHG signal from reference argon atoms. The image has been symmetrized into all four polar quadrants

This results in a normalized HHG signal. We plot the square root of this normalized signal in Fig. 10.12. This figure is somewhat different than the results shown in Fig. 10.6 for CO_2 which used linearly polarized light to generate HHG. In the present case using elliptical light, there is a small minimum at 90 degrees, whereas for linear light, there is a maximum at 90 degrees. This is probably related to the nodal plane in the HOMO wave function.

We will reconstruct the bound state wave function from this data, using a slightly different procedure than in the previous section. As before, the HHG signal is written as a product of a recombination moment times the amplitude of the recolliding electron wave packet, a.

$$S(\omega;\theta) = \left|a(\omega)\right|^2 \left|d_L(\omega;\theta)\right|^2$$

Previously we used the length form of the transition dipole matrix element between the bound state and the continuum wave function which is approximated by a plane wave.

$$d_L(\omega;\theta) = \left\langle \Psi(r;\theta)\middle|r\middle|k(\omega)\right\rangle \tag{10.7}$$

$$= \int dr \Psi(r;\theta) r e^{ikr} \tag{10.8}$$

Instead we use the velocity form of the matrix element,

$$d_v(\omega;\theta) = \Omega\left\langle \Psi(r;\theta)\middle|\hat{p}\middle|k(\omega)\right\rangle \tag{10.9}$$

$$= \Omega \int dr \Psi(r;\theta)\hat{p} e^{ikr} \tag{10.10}$$

$$= \Omega k \Psi(p;\theta) \tag{10.11}$$

since the momentum operator $\hat{p}$ operating on a plane wave of momentum k returns k. Therefore the velocity form of the transition dipole matrix element is proportional to the bound state wave function in momentum space. This is just the

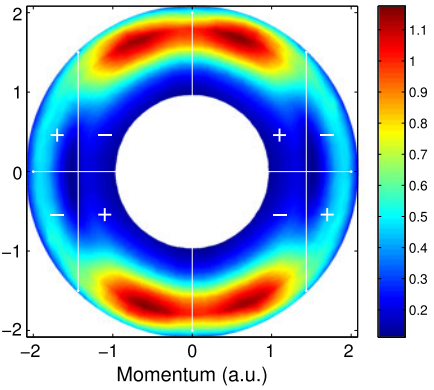

Fig. 10.13 Polar plot of the square root of the CO_2 signal from Fig. 10.11, normalized by the HHG signal from reference argon atoms, as shown in Fig. 10.12. The values have been multiplied by ± 1 in different parts of the image, corresponding to where phase jumps are assumed to occur

spatial Fourier transform of the real space wave function. This velocity form approach has the advantage that it does not require knowledge of the two polarization components of the emission; this is also a shortcoming, since it does not take into account the extra information provided by the polarization. In the present experiment using elliptically polarized light, we do not have the polarization information of the XUV radiation.

We lack one vital piece of information, namely the phase of the XUV emission. As in the case of N_2, we will assume that the wave function is real, so that the phase will be either 0 or π. Therefore we multiply the square root of the normalized signal (Fig. 10.12) by ± 1, as shown in Fig. 10.13. We assume a phase jump near H25, where there is a minimum in the emission (see Fig. 10.12). We also assume a phase jump at angle 0, 90, 180 and 270 degrees. This assumption is based on the assumption of the symmetry of the bound state wave function. By taking the inverse Fourier transform of Fig. 10.13, we arrive at the spatial image of the bound state wave function of CO_2, shown in Fig. 10.14. This indeed looks like the expected Π_g orbital of CO_2.

The problem with this orbital reconstruction is the assumption of phase jumps. By assuming phase jumps at each quadrant, we have in effect determined the symmetry of the wave function. If we do not put in a phase jump at 90 and 270 degrees, we can reconstruct an orbital with Π_u symmetry instead. In fact, if you replace the experimental data in Fig. 10.12 with the value 1 everywhere, but make the same phase change assumptions, then you still obtain an orbital that looks like a Π_g wave function. Therefore we should be very suspicious when someone uses this approach to reconstruct the CO_2 HOMO wave function.

10.7 Following a Chemical Reaction Using High-Harmonic Spectroscopy

Simultaneous imaging of the geometric and electronic structure of a molecule as it undergoes a chemical reaction is one of the main goals of modern ultrafast sci-

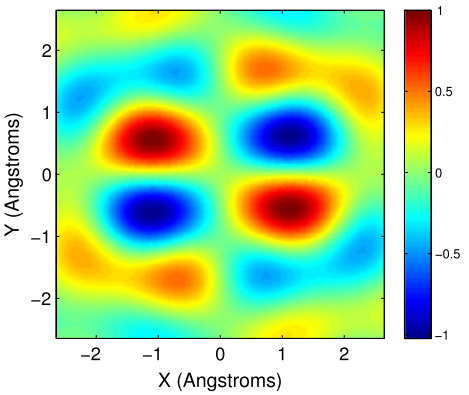

Fig. 10.14 An inverse Fourier transform of the velocity-form transition moments in Fig. 10.13 is shown. This should be a reconstructed image of the CO_2 HOMO wave function. It indeed shows the expected Π_g symmetry. Unfortunately, the symmetry of this image is determined by the assumptions of phase jumps that were made in Fig. 10.13. Other assumptions of phase jumps would lead to different symmetries

ence. Techniques based on diffraction [94, 95] measure the position of the atoms within the molecule with high accuracy but are much less sensitive to the electronic structure of the molecule, particularly the valence shell in which the chemical transformations originate. A new complementary approach exploits the rescattering of an electron removed from the molecule by a strong laser field to measure the structure of the molecule [96]. The associated recollision also leads to high-harmonic generation that encodes the structure of the orbital to which the electron recombines [3, 97]. So far, these methods have only been applied to the electronic ground state of molecules [35, 98–100]. Ultrafast dynamics in molecules occur predominantly in excited electronic states which can only be prepared in small fractions when multiphoton processes need to be avoided.

We extend high-harmonic spectroscopy from probing static molecular structure to probing photochemical dynamics. Using the impulsive photodissociation of molecular bromine, we show that the electromagnetic interference between high harmonics generated from the molecular ground state and the excited state occurs on the attosecond timescale. The coherent addition of the emitted radiation results in high visibility of the excited state dynamics despite the low excited state fraction.

The photorecombination step in high-harmonic generation is essentially a time reversal of photoionization. Before describing the HHG experiment, it is useful to compare and contrast the two approaches. In femtosecond photoelectron spectroscopy, single-photon absorption creates a photoelectron which encodes information of the molecule's electronic structure in its spectrum [101, 102]. In femtosecond high-harmonic spectroscopy, similar detailed information [23, 43] is carried in the emitted photon. In photoelectron spectroscopy, different initial (neutral) and final (ionic) electronic states are distinguished through the photoelectron energy. In high-harmonic spectroscopy, the broadband recolliding electron wave can only re-

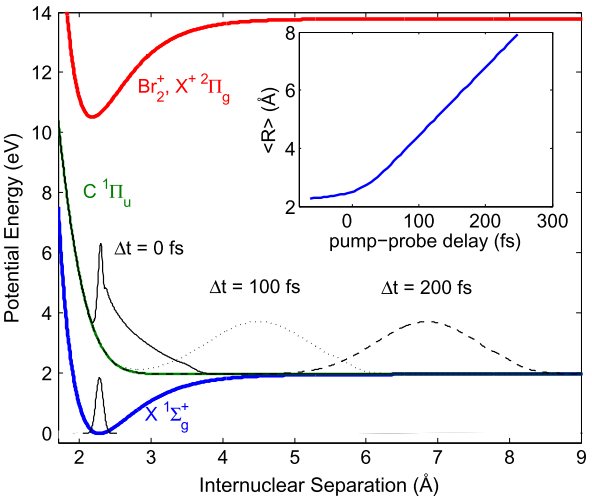

Fig. 10.15 Potential energy curves of Br_2 ($X\ ^1\Sigma_g^+$ ground state and $C\ ^1\Pi_{1u}$ excited state) and Br_2^+ ($X^+\ ^2\Pi_g$ ground state). The shape of the nuclear wave packet in the excited state after selected delays Δt is also shown. The wave packets were obtained by numerical propagation assuming a 40 fs excitation pulse centered at 400 nm. *The inset* shows the expectation value of the internuclear separation as a function of the pump-probe delay. Derived from [105]

combine to vacant states, which are selectively created by the tunnel ionization step. Tunnel ionization is exponentially sensitive to the binding energy of each ionization channel. The simultaneous measurement of a broad photon spectrum and the selection of the probed state by tunneling both point to greater simplicity for high-harmonic spectroscopy. However, the emitted photons originating from different initial electronic states overlap spectrally, adding an undesirable complexity to the interpretation of high-harmonic spectroscopy. We show that this apparent complexity becomes an advantage as the unexcited molecules can serve as a local oscillator against which we measure the excited state dynamics. Just as in a radio receiver, the local oscillator makes a weak signal that would be otherwise difficult to observe, readily visible. Moreover, the coherent detection provides a high sensitivity to the phase of the radiation, which reflects the evolution of the ionization potential along the dissociation coordinate.

The experimental setup consists of a chirped-pulse amplified titanium-sapphire femtosecond laser system, a high-harmonic source chamber equipped with a pulsed valve and an XUV spectrometer. The laser system provides 800 nm pulses of 32 fs duration (FWHM). The laser beam is split into two parts of variable intensities using a half-wave plate and a polarizer. The minor part of the energy is sent through a 2:1 telescope and used to generate 400 nm radiation in a type I BBO of 60 μm thickness. The major part is sent through a computer-controlled delay stage and is recombined with the 400 nm radiation using a dichroic beam splitter. The combined beams are focused into the chamber using a $f = 50$ cm spherical mirror.

High-order harmonics are generated in a supersonic expansion of Br_2 seeded in 2 bars of helium. The helium carrier gas is sent through liquid Br_2 kept at room temperature. Bromine molecules are excited by single-photon absorption at 400 nm to the repulsive $C\ ^1\Pi_{1u}$ state (see Fig. 10.15) and high harmonics are generated in the strong 800 nm field. The focus of both beams is placed $\sim$1 mm before the pulsed molecular jet expanding through a nozzle of 250 μm diameter. This setup

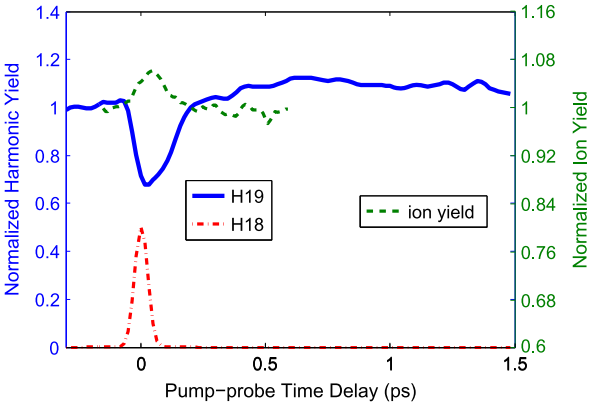

Fig. 10.16 Intensity of harmonics 19 (*full line*) and 18 (*dash-dotted line*) from excited bromine molecules as a function of the delay between a 400 nm pump pulse and a perpendicularly polarized 800 nm pulse generating high harmonics (*left-hand axis*). The temporal overlap of 400 and 800 nm pulses leads to the emission of even order harmonics, like H18. The total ion yield (*dotted line*, *right-hand axis*) shown as *dashed line* was measured under identical conditions but with higher statistics. Derived from [105]

minimizes the effect of phase-mismatch and reabsorption of the high-harmonic radiation and leads to the observation of the single-molecule response [103]. The typical pulse energies of 1.5 mJ (800 nm) and 5 μJ (400 nm) result in intensities of 1.5×10^{14} W/cm^2 (800 nm) and 5×10^{11} W/cm^2, the 400 nm beam having half the diameter of the 800 nm beam. The total number of produced ions is measured by a wire mesh located 10 cm below the nozzle orifice. We have verified that the response of the ion detector was linear. The high-harmonics are spectrally resolved using an aberration-corrected XUV grating and imaged by a micro-channel plate detector backed with a phosphor screen using a charge-coupled device camera. The harmonic intensities are extracted by integrating the images spatially and spectrally.

Figure 10.15 shows the relevant potential energy curves of Br_2 and Br_2^+. Single-photon excitation at 400 nm from the X $^1\Sigma_g^+$ ground state leads almost exclusively to the repulsive C $^1\Pi_{1u}$ state which dissociates into two bromine atoms in their ground spin-orbit state ($^2P_{3/2}, m_J = 1/2$) [104]. The figure also shows the shape of the vibrational wave function in the ground state and the calculated nuclear wave packet on the excited state surface at selected delays Δt after excitation by a 40 fs pump pulse centered at 400 nm. The $^2\Pi_{3/2g}$ ground state curve of Br_2^+ is also shown to illustrate the variation of the ionization potential with the internuclear distance.

Figure 10.16 shows the observed harmonic and ion signals in a pump-probe experiment with perpendicular polarizations. The power of H19 decreases during the excitation, reaches a minimum after the peak of the 400 nm pulse and then recovers to its initial power level. In contrast, the ion yield increases, reaching its maximum after the peak of the 400 nm pulse and subsequently decreases to its initial level. The maximum increase in ion yield amounts to 7 % whereas the harmonic signal is depleted by up to 30 %. The signal of H19 and the ion yield have been normalized to

unity at negative delays. This signal level corresponds to all molecules being in the ground electronic state. Temporal overlap of the 800 nm and 400 nm pulses leads to the appearance of even-order harmonics [106] which provide the time origin and a high-order cross-correlation (∼50–60 fs).

When Br_2 is excited to the C $^1\Pi_{1u}$ state, the ionization potential for the removal of the most weakly bound electron is reduced from 10.5 to 7.5 eV, explaining the observed increase in the ion yield. The rising part of the ion yield curve reflects the build-up of the excited state population during the excitation pulse. As Br_2 dissociates along the repulsive C $^1\Pi_{1u}$ state, the ionization potential increases from 7.5 to 11.8 eV, resulting in a decreasing ionization rate of the excited state. Since the ionization rate increases at early delays, one might expect that the harmonic yield would also increase. However, the opposite is observed. Moreover, the variation of the harmonic signal is much larger than that of the ion signal and exceeds the excitation fraction by a factor of 2.

These results clearly demonstrate a destructive interference between harmonics emitted by the excited molecules and those emitted by the ground state molecules. Destructive interference is the origin of the opposite behavior of ion and harmonic yield. Since the interference between the excited and unexcited molecules involves both phase and amplitude of emission, it is impossible to determine both parameters with a single measurement. In the following section, we utilize a different geometry in order to extract both amplitude and phase.

10.8 Transient Grating High Harmonic Spectroscopy

The strong-field approach to molecular imaging relies on an intense femtosecond laser field ($\sim 10^{14}$ W/cm^2) to extract an electron wave packet from one of the valence orbitals and drive it back to interfere with the initial bound electronic state. When the electron recombines with the parent ion, it emits extreme-ultraviolet (XUV) radiation in a train of attosecond pulses. All molecules in the sample radiate coherently with the electric field of the driving laser in a phase-matched process. In this section, we demonstrate how HHG can be applied to observe a chemical reaction in real time [89, 107].

We form a sinusoidal grating of excited molecules using two pump beams that cross in the medium, as shown in Fig. 10.17. Horizontal planes of excited molecules alternate with planes of unexcited molecules. We generate high harmonics from this grating with a delayed 800 nm laser pulse (probe). The zero time-delay and the cross-correlation time of 50 fs is monitored through the appearance of even-order harmonics.

From the zeroth and first order diffracted signals, we can uniquely extract the harmonic amplitudes d_e/d_g and phases $|\phi_e - \phi_g|$ of the excited state relative to the ground state (where $d_{g,e}$ and $\phi_{g,e}$ are the harmonic amplitudes and phases of the ground (g) and excited (e) states). We show the experimentally determined values in Fig. 10.18, when the pump and probe pulses are parallel (a) or perpendicular (b).

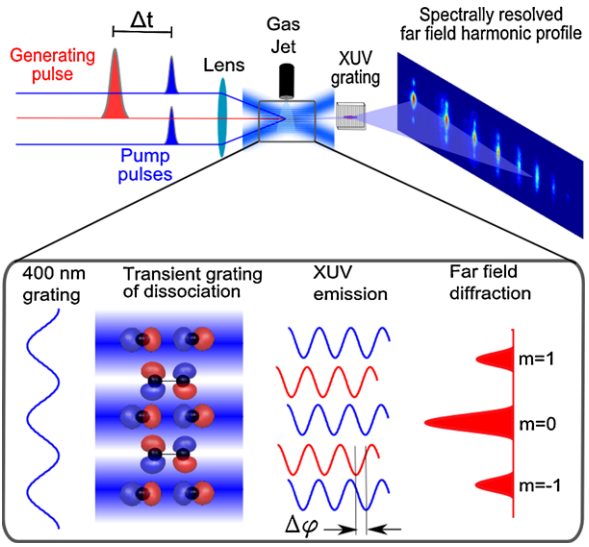

Fig. 10.17 Schematic of the transient grating excitation geometry. Two 400 nm pump pulses set up a transient grating of excitation in the molecular beam. A delayed 800 nm pulse generates high harmonics. The periodic modulation of the high harmonic amplitude and phase in the near field results in first order diffraction in the far field. Derived from [107]

The different time evolution for the amplitude and the phase is striking. While the phase reaches its asymptotic value after ≈150 fs, the amplitude takes more than 300 fs. It is also striking that the time response of the amplitude changes with the relative polarization of the excitation and harmonic generation pulse. In contrast, while the time-dependent phase is different for the different polarizations, it reaches the same asymptotic value at the same time delay. We will first concentrate on the phase, then discuss the amplitude.

The phase of high-harmonic radiation has two main contributions: (1) The electron and the ion accumulate a relative phase between the moment of ionization and recombination. The phase shift between the same harmonic order q being emitted by two electronic states differing in ionization potential by ΔI_p can be expressed as $\Delta\phi_q \approx \Delta I_p \bar{\tau}_q$, [25] where $\bar{\tau}_q$ is the average transit time of the electron in the continuum. (2) When the electron recombines, the transition moment imposes an amplitude and a phase on the radiation [11, 23]. The first contribution depends on the electron trajectory (determined by the laser parameters) and the ionization potential. The second contribution characterises the electronic structure of the molecule. It depends on the emitted photon energy and the angle of recombination in the molecular frame [3].

The time evolution of the reconstructed phase in Fig. 10.18 can be split in two regions: the first 150 fs, where the phase undergoes a rapid variation, and the subsequent flat region where the phase is independent of the relative polarizations. The rapid variation of the phase reflects the fast variation of the ionization potentials with delay. The strong dependence of the phase on the relative polarizations (Fig. 10.18(a) vs. (b)) also shows that the phase traces the evolution of the electronic structure of the molecule as it dissociates. This variation occurs because the electrostatic potential into which the electron recombines changes significantly. At asymptotic delays we measure Br atoms relative to ground state molecules. The

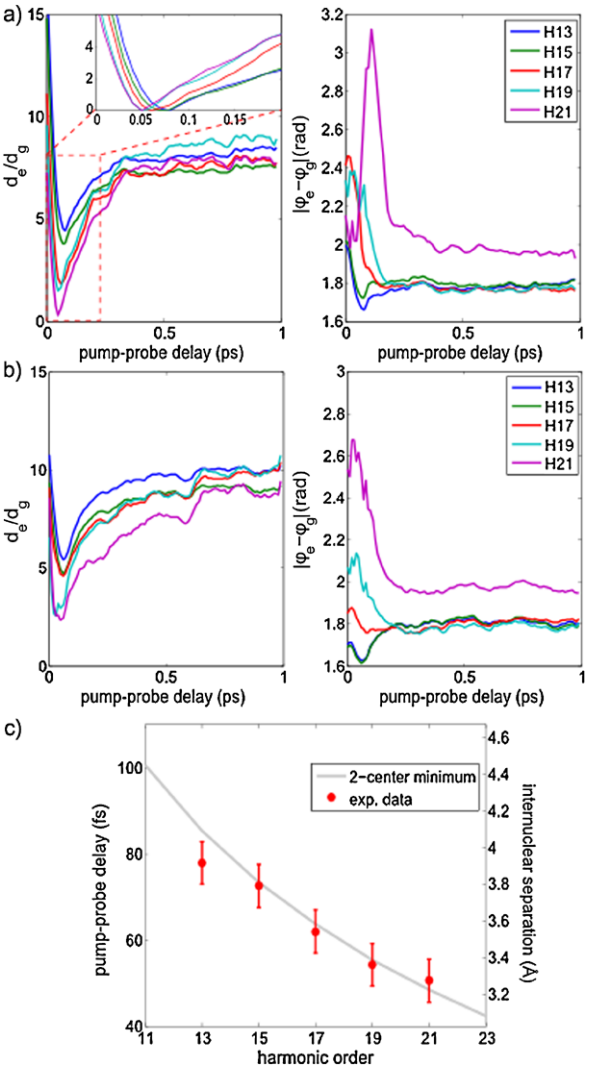

Fig. 10.18 Reconstruction of high harmonic amplitude and phase. (**a**) shows the reconstructed amplitude (*left*) and phase (*right*) of the excited state emission relative to the ground state, for parallel pump-probe polarizations. (**b**) is the same as (**a**) except the pump-probe polarizations are perpendicular. (**c**) shows the measured internuclear separations as determined by the two-center interference condition for each harmonic order. Derived from [107]

phase shift is independent of the direction of recombination, consistent with the fact that Br_2 dissociates into atoms in the $|m_j| = 1/2$ magnetic sub-level [104]. The phase shift is 1.8 radians for H13. Using the relation $\Delta\phi_q \approx \Delta I_p \bar{\tau}_q$, we obtain $\Delta I_p = 1.3$ eV, in good agreement with the known ionization potentials of Br_2 and Br.

We now turn to the temporal evolution of the amplitudes. The odd harmonics go through a deep minimum at an early time delay that depends on the harmonic order (see inset of Fig. 10.18(a)). The minimum occurs between 51 ± 5 fs (H21) and 78 ± 5 fs (H13). It measures the stretching of the orbital as the molecule dissociates. Since at early delays the ionization step selects molecules lying parallel to the

laser field, we obtain almost identical results in both polarizations. When the electron recombines to the initial state, its de Broglie wavelength λ_q can destructively interfere with the initial state wave function. Destructive interference occurs when $R = (2n + 1)/2\lambda_q$ (n integer) in the case of a σ_u orbital [24]. Using $n = 1$ and the relation $\Omega = k^2/2$ between the photon energy Ω and the electron momentum k, we translate the minimum of H21 to a bond length of 3.3 Å and that in H13 to 3.9 Å—in good agreement with wave packet calculations. Thus, we trace the bond length as a function of time using quantum interference.

As the molecule dissociates, additional minima corresponding to destructive interference with $n > 1$ could be expected. Instead, we observe a slow rise of the amplitude. At delays larger than 150 fs, the four valence molecular orbitals of Br_2 formed from the 4p atomic orbitals of Br become nearly degenerate and high-harmonic generation becomes essentially atomic in character. In this regime, the gerade or ungerade states of the ion are degenerate—there should be no quantum interference in ionization nor in recombination. Consequently, it is only the propagation of the electron in the laser field that is affected by the second atom. For perpendicularly polarised pump and probe beams, the interaction of the ionised electron with the neighbouring atom is maximized since the electron trajectory between tunneling and recollision lies in the plane of the disc of dissociating atoms. The slower recovery of the amplitude in Fig. 10.18(b) reflects this fact. This property of high-harmonic spectroscopy is analogous to XAFS (extended X-ray absorption fine structure) and may be useful to probe the chemical environment of a low-I_p species (e.g. a molecule in a helium droplet).

Time-resolved photoelectron measurements of the dissociation of Br_2 have beautifully demonstrated how the binding energies shift as the atoms move apart. In Refs. [102, 108, 109] the time delay for the appearance of an atomic-like photoelectron spectrum was determined to lie in the range of 40–85 fs. In high-harmonic spectroscopy, the recollision of the returning photoelectron is sensitive to the electronic structure of the molecule rather than to the binding energy of individual orbitals. The minima between 50–80 fs show that the electron recombines to a 2-centre molecular wave function. The absence of such minima in the range of 100–150 fs suggests that at longer delays the recombination of the electron has become essentially atomic. An analogous transition between two- and one-center signatures has recently been observed in core-shell photoionization of a static molecule [110].

Looking forward, measuring the amplitude and phase of the photorecombination moment relative to a fully characterised ground state reference [3] will allow the dynamic imaging of orbitals in a chemical reaction. The unique properties of high-harmonic spectroscopy will lead to other applications in femtochemistry, reaching from simple dissociation dynamics, to proton transfer, to non-adiabatic reaction dynamics, to complex photochemical processes. For example, the change in electronic structure associated with the crossing of a conical intersection [111, 112] will be mapped into the harmonic radiation. In all these cases, the sensitivity of high harmonic spectroscopy to the electronic structure will provide new insight.

10.9 Conclusions

We hope that the reader will recognize the potential of this new spectroscopic technique called high harmonic spectroscopy. We have shown that we can observe electronic structure in atoms and molecules, that we can reconstruct a single molecular orbital wave function, and that we can follow a chemical reaction. As we gain experience with this technique, we learn its advantages and disadvantages. We have recently observed that high harmonic spectroscopy with molecules larger than diatomics is sensitive to the electronic state of the excited molecule, rather than the motion of a nuclear wavepacket; we have shown this for NO_2 [113] and recently for SO_2, and we believe that this may be a general property. We expect that the advent of mid-infrared few-cycle laser sources will also help in applying high harmonic spectroscopy to larger molecules with low ionization potentials.

References

1. E. Goulielmakis, M. Schultze, M. Hofstetter, V.S. Yakovlev, J. Gagnon, M. Uiberacker, A.L. Aquila, E.M. Gullikson, D.T. Attwood, R. Kienberger, F. Krausz, U. Kleineberg, Single-cycle nonlinear optics. Science **320**(5883), 1614 (2008). doi:10.1126/science.1157846
2. S. Baker, J.S. Robinson, C.A. Haworth, H. Teng, R.A. Smith, C.C. Chirila, M. Lein, J.W.G. Tisch, J.P. Marangos, Science **312**, 424 (2006)
3. J. Itatani, J. Levesque, D. Zeidler, H. Niikura, H. Pépin, J.C. Kieffer, P.B. Corkum, D.M. Villeneuve, Nature (London) **432**, 867 (2004)
4. P.B. Corkum, Phys. Rev. Lett. **71**, 1994 (1993)
5. H. Niikura, F. Légaré, R. Hasbani, A.D. Bandrauk, M.Y. Ivanov, D.M. Villeneuve, P.B. Corkum, Nature **417**, 917 (2002)
6. Committee on AMO2010, *Controlling the Quantum World: The Science of Atoms, Molecules and Photons* (The National Academies Press, Washington, 2006)
7. J. Berkowitz, *Photoabsorption, Photoionization and Photoelectron Spectroscopy* (Academic Press, New York, 1979)
8. K. Kimura, S. Katsumata, Y. Achiba, T. Yamazaki, S. Iwata, *Handbook of HeI Photoelectron Spectra* (Japan Scientific Societies Press, Tokyo, 1981)
9. U. Becker, D.A. Shirley (eds.), *VUV and Soft X-Ray Photoionization* (Plenum, New York, 1996)
10. R. Torres, N. Kajumba, J.G. Underwood, J.S. Robinson, S. Baker, J.W.G. Tisch, R. de Nalda, W.A. Bryan, R. Velotta, C. Altucci, I.C.E. Turcu, J.P. Marangos, Phys. Rev. Lett. **98**(20), 203007 (2007)
11. O. Smirnova, Y. Mairesse, S. Patchkovskii, N. Dudovich, D. Villeneuve, P. Corkum, M.Y. Ivanov, Nature (London) **460**(7258), 972 (2009)
12. H.J. Wörner, J.B. Bertrand, D.V. Kartashov, P.B. Corkum, D.M. Villeneuve, Nature (London) **466**, 604 (2010)
13. H.J. Wörner, H. Niikura, J.B. Bertrand, P.B. Corkum, D.M. Villeneuve, Phys. Rev. Lett. **102**(10), 103901 (2009). doi:10.1103/PhysRevLett.102.103901
14. A.-T. Le, R.R. Lucchese, M.T. Lee, C.D. Lin, Phys. Rev. Lett. **102**(20), 203001 (2009)
15. M.V. Frolov, N.L. Manakov, T.S. Sarantseva, M.Y. Emelin, M.Y. Ryabikin, A.F. Starace, Phys. Rev. Lett. **102**(24), 243901 (2009). doi:10.1103/PhysRevLett.102.243901
16. M. Lewenstein, P. Balcou, M.Y. Ivanov, A. L'huillier, P.B. Corkum, Phys. Rev. A **49**, 2117 (1994). doi:10.1103/PhysRevA.49.2117

17. O. Smirnova, M. Spanner, M. Ivanov, Phys. Rev. A **77**(3), 033407 (2008). doi:10.1103/PhysRevA.77.033407
18. Z.B. Walters, S. Tonzani, C.H. Greene, J. Phys. B **40**(18), 277 (2007)
19. T. Morishita, A.-T. Le, Z. Chen, C.D. Lin, Phys. Rev. Lett. **100**(1), 013903 (2008). doi:10.1103/PhysRevLett.100.013903
20. M.F. Ciappina, C.C. Chirila, M. Lein, Phys. Rev. A **75**(4), 043405 (2007). doi:10.1103/PhysRevA.75.043405
21. J.W. Cooper, Phys. Rev. **128**, 681 (1962)
22. J.S. Robinson, C.A. Haworth, H. Teng, R.A. Smith, J.P. Marangos, J.W.G. Tisch, Appl. Phys. B **85**, 525 (2006)
23. H.J. Wörner, H. Niikura, J.B. Bertrand, P.B. Corkum, D.M. Villeneuve, Phys. Rev. Lett. **102**(10), 103901 (2009)
24. M. Lein, N. Hay, R. Velotta, J.P. Marangos, P.L. Knight, Phys. Rev. Lett. **88**, 183903 (2002)
25. T. Kanai, E.J. Takahashi, Y. Nabekawa, K. Midorikawa, Phys. Rev. Lett. **98**, 153904 (2007)
26. P. Colosimo, G. Doumy, C.I. Blaga, J. Wheeler, C. Hauri, F. Catoire, J. Tate, R. Chirla, A.M. March, G.G. Paulus, H.G. Muller, P. Agostini, L.F. Dimauro, Nat. Phys. **4**, 386 (2008)
27. J.A.R. Samson, W.C. Stolte J. Electron Spectrosc. Relat. Phenom. **123**, 265 (2002)
28. A. L'Huillier, P. Balcou, Phys. Rev. Lett. **70**, 774 (1993)
29. S. Minemoto, T. Umegaki, Y. Oguchi, T. Morishita, A.-T. Le, S. Watanabe, H. Sakai, Phys. Rev. A **78**(6), 061402 (2008)
30. H.G. Muller, Phys. Rev. A **60**, 1341 (1999)
31. D.J. Tannor, *Introduction to Quantum Mechanics: A Time-Dependent Perspective* (University Science Books, Sausalito, 2007)
32. A.F. Starace, Theory of atomic photoionization, in *Handbuch der Physik*, vol. 31, ed. by W. Mehlhorn (Springer, Berlin, 1981), pp. 1–121
33. P.M. Paul, E.S. Toma, P. Breger, G. Mullot, F. Augé, P. Balcou, H.G. Muller, P. Agostini, Science **292**, 1689 (2001)
34. Y. Mairesse, A. de Bohan, L.J. Frasinski, H. Merdji, L.C. Dinu, P. Monchicourt, P. Breger, M. Kovacev, R. Taieb, B. Carré, H.G. Muller, P. Agostini, P. Salières, Science **302**, 1540 (2003)
35. C. Vozzi, F. Calegari, E. Benedetti, J.-P. Caumes, G. Sansone, S. Stagira, M. Nisoli, R. Torres, E. Heesel, N. Kajumba, J.P. Marangos, C. Altucci, R. Velotta, Phys. Rev. Lett. **95**(15), 153902 (2005). doi:10.1103/PhysRevLett.95.153902
36. J. Levesque, D. Zeidler, J.P. Marangos, P.B. Corkum, D.M. Villeneuve, Phys. Rev. Lett. **98**(18), 183903 (2007). doi:10.1103/PhysRevLett.98.183903
37. R.A. Ganeev, J. Phys. B, At. Mol. Phys. **40**, R213 (2007). doi:10.1088/0953-4075/40/22/R01
38. M.V. Frolov, N.L. Manakov, A.F. Starace, Phys. Rev. A **82**(2), 023424 (2010). doi:10.1103/PhysRevA.82.023424
39. A.D. Shiner, B. Schmidt, C. Trallero-Herrero, H.J. Wörner, S. Patchkovskii, P.B. Corkum, J.-C. Kieffer, F. Légaré, D.M. Villeneuve, Nat. Phys. **7**(7), 464 (2011)
40. M. Giguère, B.E. Schmidt, A.D. Shiner, M.-A. Houle, H.C. Bandulet, G. Tempea, D.M. Villeneuve, J.-C. Kieffer, F. Légaré, Opt. Lett. **34**(12), 1894 (2009)
41. B.E. Schmidt, P. Béjot, M. Giguère, A.D. Shiner, C. Trallero-Herrero, É. Bisson, J. Kasparian, J. Wolf, D.M. Villeneuve, J. Kieffer, P.B. Corkum, F. Légaré, Appl. Phys. Lett. **96**(12), 121109 (2010). doi:10.1063/1.3359458
42. B.E. Schmidt, A.D. Shiner, P. Lassonde, J.-C. Kieffer, P.B. Corkum, D.M. Villeneuve, F. Légaré, Opt. Express **19**, 6858 (2011)
43. A.-T. Le, R.R. Lucchese, S. Tonzani, T. Morishita, C.D. Lin, Phys. Rev. A **80**(1), 013401 (2009). doi:10.1103/PhysRevA.80.013401
44. M.V. Frolov, N.L. Manakov, T.S. Sarantseva, A.F. Starace, J. Phys. B, At. Mol. Opt. Phys. **42**(3), 035601 (2009)
45. L.D. Landau, E.M. Lifshitz, *Quantum Mechanics Non-relativistic Theory*, 3rd edn. Course of Theoretical Physics, vol. 3 (Pergamon, New York, 1977), p. 553

46. K.-N. Huang, W.R. Johnson, K.T. Cheng, At. Data Nucl. Data Tables **26**(1), 33 (1981). doi:10.1016/0092-640X(81)90010-3
47. M. Kutzner, V. Radojević, H.P. Kelly, Phys. Rev. A **40**(9), 5052 (1989). doi:10.1103/PhysRevA.40.5052
48. A. Fahlman, M.O. Krause, T.A. Carlson, A. Svensson, Phys. Rev. A **30**(2), 812 (1984). doi:10.1103/PhysRevA.30.812
49. U. Becker, D. Szostak, H.G. Kerkhoff, M. Kupsch, B. Langer, R. Wehlitz, A. Yagishita, T. Hayaishi, Phys. Rev. A **39**(8), 3902 (1989). doi:10.1103/PhysRevA.39.3902
50. M.Y. Amusia, J.-P. Connerade, Rep. Prog. Phys. **63**, 41 (2000)
51. R. Torres, N. Kajumba, J.G. Underwood, J.S. Robinson, S. Baker, J.W.G. Tisch, R. de Nalda, W.A. Bryan, R. Velotta, C. Altucci, I.C.E. Turcu, J.P. Marangos, Phys. Rev. Lett. **98**, 203007 (2007)
52. X.X. Zhou, X.M. Tong, Z.X. Zhao, C.D. Lin, Phys. Rev. A **71**, 061801 (2005)
53. X.X. Zhou, X.M. Tong, Z.X. Zhao, C.D. Lin, Phys. Rev. A **72**, 033412 (2005)
54. T. Morishita, A.-T. Le, Z. Chen, C.D. Lin, Phys. Rev. Lett. **100**, 013903 (2008)
55. M. Lein, J. Phys. B **40**, 135 (2007)
56. Y. Mairesse, J. Levesque, N. Dudovich, P.B. Corkum, D.M. Villeneuve, J. Mod. Opt. **55**(16), 2591 (2008)
57. J. Itatani, D. Zeidler, J. Levesque, M. Spanner, D.M. Villeneuve, P.B. Corkum, Phys. Rev. Lett. **94**, 123902 (2005)
58. F. Rosca-Pruna, M.J.J. Vrakking, Phys. Rev. Lett. **87**, 153902 (2001)
59. P.W. Dooley, I. Litvinyuk, K.F. Lee, D.M. Rayner, M. Spanner, D.M. Villeneuve, P.B. Corkum, Phys. Rev. A **68**, 023406 (2003)
60. M.W. Schmidt, K.K. Baldridge, J.A. Boatz, S.T. Elbert, M.S. Gordon, J.J. Jensen, S. Koseki, N. Matsunaga, K.A. Nguyen, S. Su, T.L. Windus, M. Dupuis, J.A. Montgomery J. Comput. Chem. **14**, 1347 (1993)
61. D. Pavicic, K.F. Lee, D.M. Rayner, P.B. Corkum, D.M. Villeneuve, Phys. Rev. Lett. **98**, 243001 (2007)
62. M. Lein, N. Hay, R. Velotta, J.P. Marangos, P.L. Knight, Phys. Rev. A **66**(2), 023805 (2002)
63. C. Vozzi, F. Calegari, E. Benedetti, J.-P. Caumes, G. Sansone, S. Stagira, M. Nisoli, R. Torres, E. Heesel, N. Kajumba, J.P. Marangos, C. Altucci, R. Velotta, Phys. Rev. Lett. **95**, 153902 (2005)
64. T. Kanai, S. Minemoto, H. Sakai, Nature **435**, 470 (2005)
65. W. Boutu, S. Haessler, H. Merdji, P. Breger, G. Waters, M. Stankiewicz, L.J. Frasinski, R. Taieb, J. Caillat, A. Maquet, P. Monchicourt, B. Carre, P. Salieres, Nat. Phys. **4**(7), 545 (2008)
66. H.J. Wörner, J.B. Bertrand, P. Hockett, P.B. Corkum, D.M. Villeneuve, Phys. Rev. Lett. **104**(23), 233904 (2010). doi:10.1103/PhysRevLett.104.233904
67. H. Wabnitz, Y. Mairesse, L.J. Frasinski, M. Stankiewicz, W. Boutu, P. Breger, P. Johnsson, H. Merdji, P. Monchicourt, P. Salières, K. Varju, M. Vitteau, B. Carré, Eur. Phys. J. D **40**, 305 (2006)
68. J. Levesque, Y. Mairesse, N. Dudovich, H. Pépin, J.-C. Kieffer, P.B. Corkum, D.M. Villeneuve, Phys. Rev. Lett. **99**(24), 243001 (2007)
69. P. Antoine, B. Carré, A. L'Huillier, M. Lewenstein, Phys. Rev. A **55**(2), 1314 (1997)
70. Y. Mairesse, S. Haessler, B. Fabre, J. Higuet, W. Boutu, P. Breger, E. Constant, D. Descamps, E. Mével, S. Petit, P. Salières, New J. Phys. **10**, 025028 (2008)
71. W.H.E. Schwarz, Angew. Chem., Int. Ed. Engl. **45**, 1508 (2006)
72. C.E. Brion, G. Cooper, Y. Zheng, I.V. Litvinyuk, I.E. McCarthy, Chem. Phys. **270**, 13 (2001)
73. M.F. Crommie, C.P. Lutz, D.M. Eigler Science **262**, 218 (1993)
74. L.C. Venema, J.W.G. Wildöer, J.W. Janssen, S.J. Tans, H.L.J.T. Tuinstra, L.P. Kouwenhoven, C. Dekker, Science **283**, 52 (1999)
75. J.I. Pascual, J. Gómez-Herrero, C. Rogero, A.M. Baró, D. Sánchez-Portal, E. Artacho, P. Ordejón, J.M. Soler, Chem. Phys. Lett. **321**, 78 (2000)
76. E.K.U. Gross, R.M. Dreizler, *Density Functional Theory* (Plenum Press, New York, 1995)

77. M. Lein, N. Hay, R. Velotta, J.P. Marangos, P.L. Knight, Phys. Rev. Lett. **88**, 183903 (2002)
78. M. Lein, P.P. Corso, J.P. Marangos, P.L. Knight, Phys. Rev. A **67**, 23819 (2003)
79. H. Stapelfeldt, T. Seideman, Rev. Mod. Phys. **75**, 543 (2003)
80. J.J. Larsen, K. Hald, N. Bjerre, H. Stapelfeldt, T. Seideman, Phys. Rev. Lett. **85**, 2470 (2000)
81. J.G. Underwood, M. Spanner, M.Y. Ivanov, J. Mottershead, B.J. Sussman, A. Stolow, Phys. Rev. Lett. **90**, 223001 (2003)
82. P.W. Dooley, I.V. Litvinyuk, K.F. Lee, D.M. Rayner, M. Spanner, D.M. Villeneuve, P.B. Corkum, Phys. Rev. A **68**, 23406 (2003)
83. H. Sakai, S. Minemoto, H. Nanjo, H. Tanji, T. Suzuki, Phys. Rev. Lett. **90**, 083001 (2003)
84. L. Holmegaard, J.H. Nielsen, I. Nevo, H. Stapelfeldt Phys. Rev. Lett. **102**, 023001 (2009)
85. B.K. McFarland, J.P. Farrell, P.H. Bucksbaum, M. Gühr, Science **322**, 1232 (2008)
86. M. Lewenstein, P. Balcou, M.Y. Ivanov, A. L'Huillier, P.B. Corkum, Phys. Rev. A **49**, 2117 (1994)
87. A.C. Kak, M. Slaney, *Principles of Computerized Tomographic Imaging* (SIAM, Philadelphia, 2001)
88. A. Royer Found. Phys. **19**, 3 (1989)
89. V.-H. Le, A.-T. Le, R.-H. Xie, C.D. Lin, Phys. Rev. A **76**(1), 013414 (2007)
90. S. Patchkovskii, Z. Zhao, T. Brabec, D.M. Villeneuve, Phys. Rev. Lett. **97**, 123003 (2006)
91. S. Patchkovskii, Z. Zhao, T. Brabec, D.M. Villeneuve, J. Chem. Phys. **126**, 114306 (2007)
92. C. Vozzi, M. Negro, F. Calegari, G. Sansone, M. Nisoli, S. De Silvestri, S. Stagira, Nat. Phys. **7**, 822 (2011)
93. Y. Mairesse, N. Dudovich, J. Levesque, M.Y. Ivanov, P.B. Corkum, D.M. Villeneuve, New J. Phys. **10**, 025015 (2008)
94. R. Neutze, R. Wouts, D. van der Spoel, E. Weckert, J. Hajdu, Nature **406**(6797), 752 (2000)
95. H. Ihee, V.A. Lobastov, U.M. Gomez, B.M. Goodson, R. Srinivasan, C.-Y. Ruan, A.H. Zewail, Science **291**(5503), 458 (2001). doi:10.1126/science.291.5503.458
96. M. Meckel, D. Comtois, D. Zeidler, A. Staudte, D. Pavičić, H.C. Bandulet, H. Pépin, J.C. Kieffer, R. Dörner, D.M. Villeneuve, P.B. Corkum, Science **320**, 1478 (2008)
97. S. Baker, J.S. Robinson, M. Lein, C.C. Chirila, R. Torres, H.C. Bandulet, D. Comtois, J.C. Kieffer, D.M. Villeneuve, J.W.G. Tisch, J.P. Marangos, Phys. Rev. Lett. **101**(5), 053901 (2008)
98. T. Kanai, S. Minemoto, H. Sakai, Nature (London) **435**(7041), 470 (2005)
99. N.L. Wagner, A. Wüest, I.P. Christov, T. Popmintchev, X. Zhou, M.M. Murnane, H.C. Kapteyn, Proc. Natl. Acad. Sci. USA **103**(36), 13279 (2006). doi:10.1073/pnas.0605178103
100. W. Li, X. Zhou, R. Lock, S. Patchkovskii, A. Stolow, H.C. Kapteyn, M.M. Murnane, Science **322**(5905), 1207 (2008)
101. L. Nugent-Glandorf, M. Scheer, D.A. Samuels, A.M. Mulhisen, E.R. Grant, X. Yang, V.M. Bierbaum, S.R. Leone, Phys. Rev. Lett. **87**, 193002 (2001)
102. P. Wernet, M. Odelius, K. Godehusen, J. Gaudin, O. Schwarzkopf, W. Eberhardt, Phys. Rev. Lett. **103**(1), 013001 (2009). doi:10.1103/PhysRevLett.103.013001
103. A.D. Shiner, C. Trallero-Herrero, N. Kajumba, H.-C. Bandulet, D. Comtois, F. Légaré, M. Giguere, J.-C. Kieffer, P.B. Corkum, D.M. Villeneuve, Phys. Rev. Lett. **103**(7), 073902 (2009)
104. T.P. Rakitzis, T.N. Kitsopoulos, J. Chem. Phys. **116**(21), 9228 (2002)
105. H.J. Wörner, J.B. Bertrand, P.B. Corkum, D.M. Villeneuve, Phys. Rev. Lett. **105**(10), 103002 (2010). doi:10.1103/PhysRevLett.105.103002
106. H. Eichmann, A. Egbert, S. Nolte, C. Momma, B. Wellegehausen, W. Becker, S. Long, J.K. McIver, Phys. Rev. A **51**(5), 3414 (1995)
107. H.J. Wörner, J.B. Bertrand, D.V. Kartashov, P.B. Corkum, D.M. Villeneuve, Nature **466**(7306), 604 (2010). doi:10.1038/nature09185
108. L. Nugent-Glandorf, M. Scheer, D.A. Samuels, A.M. Mulhisen, E.R. Grant, X. Yang, V.M. Bierbaum, S.R. Leone, Phys. Rev. Lett. **87**(19), 193002 (2001). doi:10.1103/PhysRevLett.87.193002

109. L. Nugent-Glandorf, M. Scheer, D.A. Samuels, V.M. Bierbaum, S.R. Leone, J. Chem. Phys. **117**, 6108 (2002)
110. B. Zimmermann, D. Rolles, B. Langer, R. Hentges, M. Braune, S. Cvejanovic, O. Geszner, F. Heiser, S. Korica, T. Lischke, A. Reinkoster, J. Viefhaus, R. Dörner, V. McKoy, U. Becker, Nat. Phys. **4**(8), 649 (2008). doi:10.1038/nphys993
111. W. Domcke, D.R. Yarkony, H. Köppel (eds.), *Conical Intersections: Electronic Structure, Dynamics and Spectroscopy*. Adv. Ser. in Phys. Chem., vol. 15 (World Scientific, Singapore, 2004)
112. P.H. Bucksbaum, Science **317**(5839), 766 (2007)
113. H.J. Wörner, J.B. Bertrand, B. Fabre, J. Higuet, H. Ruf, A. Dubrouil, S. Patchkovskii, M. Spanner, Y. Mairesse, V. Blanchet, E. Mével, E. Constant, P.B. Corkum, D.M. Villeneuve, Science **334**, 208 (2011)